The structure and properties of sputter-deposited Co-Si alloy thin films

2000 J. Phys.: Condens. Matter 12 4075

(http://iopscience.iop.org/0953-8984/12/17/313)

J. Phys.: Condens. Matter **12** (2000) 4075–4089. Printed in the UK PII: S0953-8984(00)11106-3

The structure and properties of sputter-deposited Co–Si alloy thin films

J M Fallon†, C A Faunce and P J Grundy

Joule Physics Laboratory, University of Salford, Salford M5 4WT, UK

Received 18 January 2000

Abstract. The structural and magnetic properties of $Co_{1-x}Si_x$ alloy thin films in the composition range $0 < x < 0.9$ are investigated. The sputter-deposited thin films show a single phase hcp structure up to $x \sim 0.25$. For Si compositions beyond this, but with $x < 0.6$, electron diffraction implies a single amorphous phase with features in the diffraction patterns typical of a dense random packing of hard spheres (DHRPS). These alloys are ferromagnetic. For $0.6 < x < 0.8$ additional diffraction maxima are observed that suggest the formation of at least two amorphous phases. Magnetic measurements suggest the presence of thermally unstable magnetic particles. For $x > 0.7$–0.8, Co atoms are incorporated in the covalent random network structure of Si and paramagnetism is observed. A correlation of the PEELS Co L_2/L_3 edge loss intensity ratio with the effective Co moment suggests that the magnetic changes could arise from differing local environments as Si is added, rather than a change in the particle size. Compositional mapping shows that some of the films have a composition that is not spatially uniform.

1. Introduction

Nanocrystalline and amorphous transition metal–metalloid alloys provide an interesting template to study the interplay of magnetic properties, crystallographic structure and microstructural features [1–3]. They can be fabricated by rapid quenching from the liquid melt and by condensation from the vapour. Ferromagnetic melt-spun and chill block-cast alloys have found ready application as soft magnetic materials [3].

It is well known that condensation from the vapour, and particularly sputter deposition, extends the compositional range over which it is possible to obtain mutual solubility in systems that are immiscible or partially immiscible in equilibrium, and also to prepare amorphous phase(s) well away from any eutectic composition.

There are few reported investigations of the simple binary Co–Si system; more attention has been given to other binary and multinary transition metal–metalloid systems, particularly Fe-based alloys. Co and Si form an interesting binary system in that the large atomic number difference leads to high x-ray and electron contrast, whilst the substantial alloying that results from the negative heat of mixing when these elements are brought together leads to extended solubilities and to interesting interfacial effects. The study of the structures and properties of alloys prepared by co-deposition proves very informative in assisting an understanding of the nature of the interface between cobalt and silicon and the intermixing observed in multilayered thin film structures [4].

† Now with DERA, St Andrew's Road, Gt Malvern WR14 3PS, UK.

0953-8984/00/174075+15$30.00

2. Experiment

Co–Si alloy thin films were co-deposited on to both Si(001) wafer and cleaved NaCl substrates by DC magnetron sputtering from separate targets (of 99.99% purity) arranged in a cluster geometry. The deposition system obtained a base pressure of 6×10^{-6} Pa and the samples were deposited at an Ar partial pressure of 0.4 Pa. Composition was modulated by controlling the Co to Si atom arrival ratio, the deposition of Co being maintained at a fixed rate of 40 nm min^{-1} and the Si varied between 0 and 120 nm min^{-1}. The deposition time was the same for every film, 5 minutes. This method allows a correlation of the film thickness with the resulting density and microstructural changes brought about upon alloying.

High angle x-ray diffraction and x-ray reflectometry on a Siemens D5000 x-ray system fitted with a Globel mirror and graphite monochromator gave the d-spacings and the thickness/density of the films. Electron diffraction patterns and microstructural features were imaged by high resolution transmission electron microscopy using an analytical JEOL 3010 electron microscope at Salford. The average film composition was measured using x-ray energy dispersive microanalysis (EDX). The recorded incoherent scatter contribution to the electron diffraction intensity profiles was removed using a computer code Image SXM. The L_2 and L_3 atomic absorption edges from Co atoms in the alloys were measured by parallel electron energy loss spectroscopy (PEELS) on the 3010 in an attempt to infer any local environment changes with composition. Local and high resolution PEELS and EDX imaging were investigated on a JEOL FEGTEM and a VG STEM at Oxford. An AGFM was used to measure in-plane magnetic hysteresis loops at ambient room temperature.

3. Results and discussion

3.1. Structural results

3.1.1. Low angle x-ray diffraction. As increasing concentrations of Si are added to Co, x-ray reflectivity measurements, figure 1, show that the Kiessig fringe separation decreases as a result of the film thickness increasing. This thickness increase and the drop in electron density, indicated by a lower critical angle θ_c, which approaches that of the Si substrate for very high Si concentrations, both reduce the fringe amplitude and increase the rate of drop-off of intensity with angle.

The film thickness change, figure 2, is small for compositions less than a critical value of $x_c \sim 0.25$. This small effect is probably a result of Si atoms being able to occupy vacant Co sites by substitution and x_c is a value taken to be close to the solubility limit of Si in the sputtered Co in the crystalline equilibrium phase. The equilibrium solubility of Si in bulk Co is around $x = 0.15$ and somewhat smaller than the threshold value given here. This difference implies a significant presence of vacancies or defects in the deposited film. Around the critical composition, x_c, the thickness increases markedly, due to the greater number of atoms included but more so because of a likely microstructural or density change induced at this composition.

The mass density of the film ρ, obtained from the critical angle, decreases with a greater fraction of lighter Si atoms, as shown in figure 3 where measured values obtained via θ_c are compared with calculated values using a simple dilution formula:

$$\rho = \rho_{Si}(x) + \rho_{Co}(1 - x)$$

where x is the Si concentration and ρ_{Si} and ρ_{Co} are the bulk densities of Si and Co respectively. The measurement points only agree with the formula for very Si rich disordered alloys. The film density will reduce and thickness will increase with x because of several factors. The first

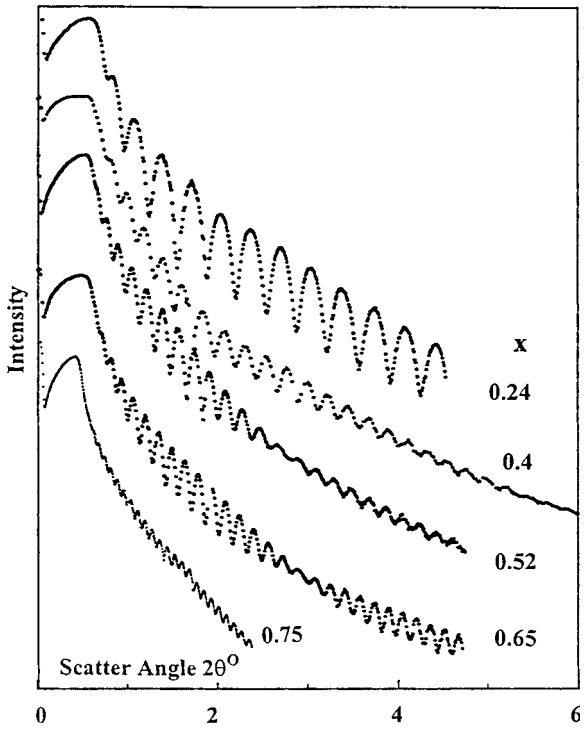

Figure 1. X-ray reflectivity curves for $Co_{1-x}Si_x$ thin film alloys. Offset and labelled in terms of x.

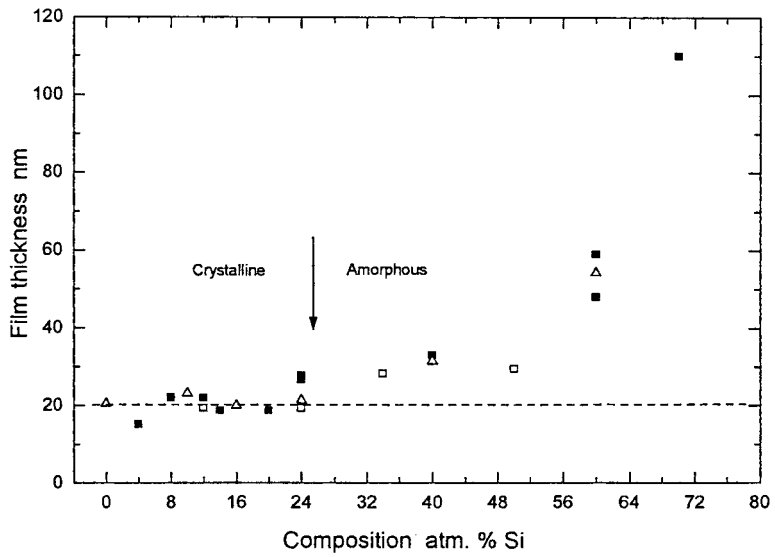

Figure 2. Dependence of thickness on composition for three sets of alloy films marked by the different symbols. Thickness values are obtained from Kiessig fringe data (some shown in figure 1). The arrow marks the approximate division between crystalline and amorphous structures.

is the greater number of lighter Si atoms included. The second is a crystalline to amorphous transformation; transition metal–metalloid alloys experience a 10% drop in density arising

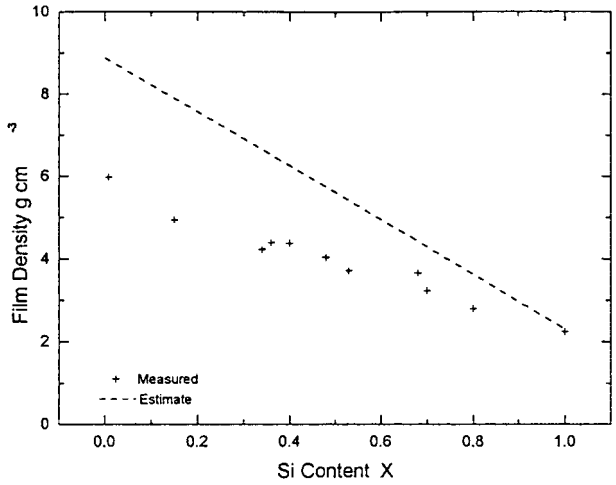

Figure 3. Showing the dependence of the mass density of the films, calculated from the critical angle θ_c taken from figure 1.

from dilation in the amorphous phase [5]. This will in turn increase the film thickness. A change from a dense random packing of hard spheres (DRPHS) to a coherent random network structure (CRN), possible at very high Si concentrations, will, however, exaggerate the thickness increase further as Co atoms are forced to take on abnormally large effective d-spacings. A third factor is the creation of voids or compositional inhomogenities in the growing film which are more likely as the adatom mobility reduces. Computer modelling of the x-ray reflectivity profiles using the SUPREX computer code [6] suggests that the r.m.s. surface roughness increases from 2 nm to 4 nm as the film thickness increases from 20 nm to 120 nm.

3.1.2. High angle x-ray diffraction. Representative x-ray patterns, offset for comparison in figure 4, show the only group of peaks detectable from the thin films. They are identified as reflections from hcp {100}, (002) and {101} planes at d-spacings close to those of hcp cobalt.

For $x < 0.22$ the hcp structure is preserved. The alloy does not appear to undergo a hcp to fcc phase change with increasing x that would, for example, cause the main peak to shift to smaller scatter angles. All peak positions remain unaltered with no change in lattice parameter indicating that any induced strains are random rather than uniform. A small, but clear, increase in the intensity of the 002 reflection with increasing Si content, compared to that from a randomly oriented pure Co film, would suggest a larger fraction of the grains with a c-axis perpendicular to the plane of the film in a definite but weak fibre texture.

For $x > 0.25$, the formation of a nanocrystalline structure or, alternatively, some significant disruption of crystal growth is implied. Most likely is a crystal distortion/amorphization process since the broad yet much more intense Bragg peaks, very typical of some nanocrystalline multilayer structures with thin Co layers [4], are never observed with co-deposited alloy films. X-ray rocking curves, figure 5, taken around the 002 reflection show that the Bragg peak width decreases and its intensity increases as the critical composition x_c ($\sim$0.25) is approached. This is further evidence to show that the films take on a weak texture with increasing Si content in the crystalline phase.

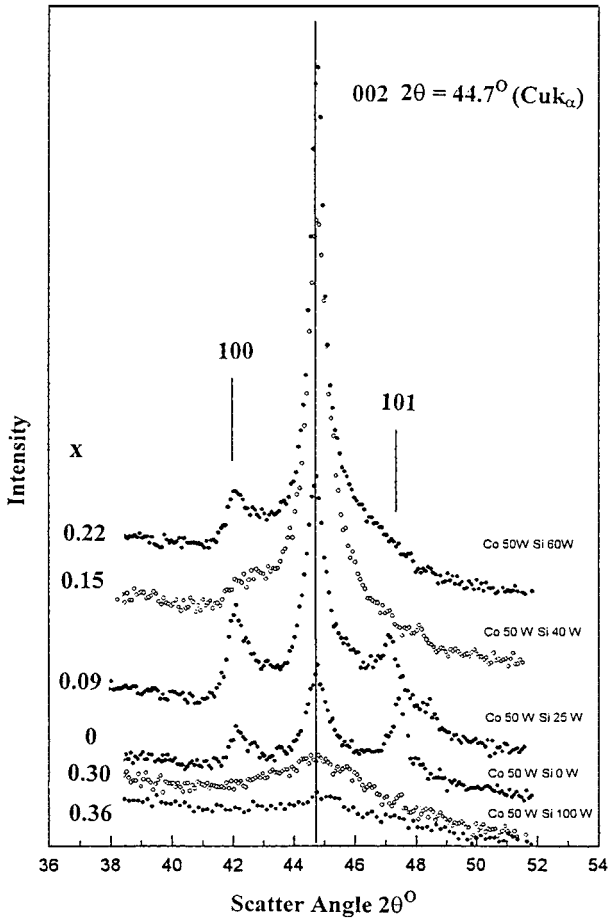

Figure 4. X-ray diffraction patterns from some alloys with $0 < x < 0.36$. The 100, 002 and 101 maxima positions are marked, as are the values of x and the powers used on the two magnetron sources.

3.1.3. Electron diffraction. Electron diffraction patterns, which remain unaltered over sampled regions at least 1000 μm^2 in area, are shown for several alloys in figures 6(a), (b), (c), (d). For $x < 0.24$ continuous diffraction rings suggest randomly orientated grains and correspond to d-spacings expected for an hcp structure with a lattice parameter near to that of bulk Co. In the composition range $0.3 < x < 0.6$, structural changes are slight and no diffraction maxima in these patterns could be matched to Co silicide compounds. Silicide formation is known to be kinetically limited at ambient temperatures. The form and spacings of the maxima in the amorphous phase resemble those from a DRPHS system [1].

The angle θ_m at which the first peak occurs for an amorphous phase is given by the Ehrenfest formula [7] $\sin\theta_m = 1.23\lambda/2d$, where λ is the wavelength of the radiation. The alloys are apparently amorphous in a CNR structure at higher concentrations, therefore, assuming a DRHPS for $x < 0.6$, the interatomic distances d are given by the hard sphere diameters, 0.125 nm and 0.128 nm for Co and Si respectively. However, it is not possible to tell or, indeed, to confirm by this method whether separate phases formed by elemental segregation, do or do not exist. This is because θ_m is predicted to be almost the same for the a-Co and a-Si phases.

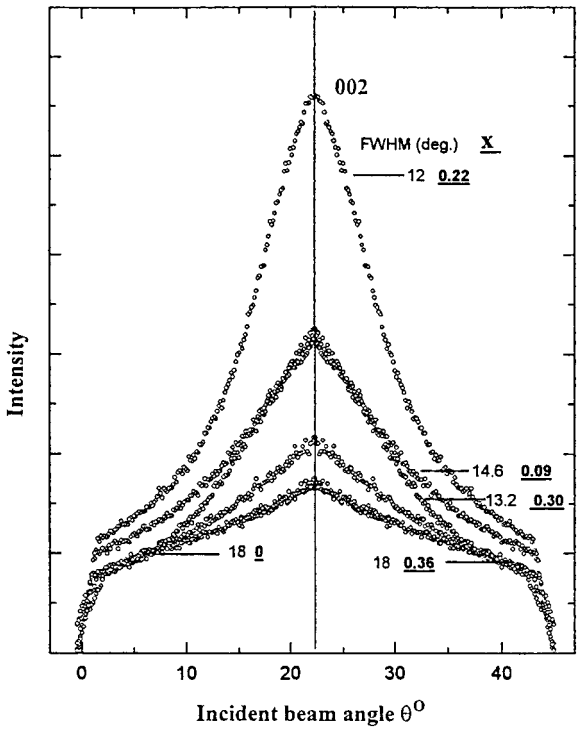

Figure 5. X-ray rocking curves taken round the 002 maximum for $0 < x < 0.36$. The profiles are labelled with the FWHM value in degrees and the value of x.

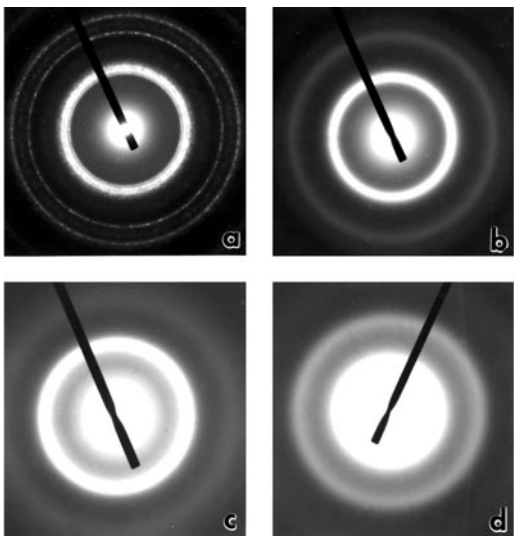

Figure 6. Transmission electron diffraction patterns for films with (a) $x = 0.24$, (b) $x = 0.46$, (c) $x = 0.68$ and (d) $x = 0.81$.

It is notable, however, that the first halos, e.g. in figures 6(b), (c), have effective d-values that are close to those for the 100, 002, 101 reflections from the crystalline Co hcp phase. This suggests that the scattering objects responsible for the main halo in this composition range

Table 1. Diameter and intensity ratios of electron diffraction maxima.

	S_2/S_1	S_3/S_1	S_4/S_1	I_1/I_2	I_1/I_3
DRPHS	1.73	1.86–1.9	2.5		
a-NiP [8]	1.67	1.94	2.44	7	14
$Co_{1-x}Si_x$					
$x = 0.34$	1.67	1.96	2.44	7.8	16.8
$x = 0.47$	1.66	1.97	2.48	7.7	12.8
$x = 0.54$	1.68	2.01	2.48	8.5	15.3

are the nearest neighbour Co atoms. Most single phase amorphous transition metal–metalloid alloys e.g. $Ni_{1-x}P_x$ [8] with around $x = 0.20$ have effective d-values which are close to the crystalline phase of the transition metal.

The second halo, figure 6(b), contains a shoulder that remains over the broad composition range $0.3 < x < 0.6$. This is taken to imply that the average short range order continues to be well defined. This is usually the case with other transition metal–metalloid combinations prepared by rapid quenching from the melt, e.g. in Ni–P [8] and $(Ni_{50}Pd_{50})_{100-x}P_x$ [9], or by electro-deposition e.g. Co–P [10] where the peak splitting occurs over a very narrow composition range (∼10%) centred around 20% metalloid. The apparent difference between the sputter-deposited alloys reported on here and these rapidly quenched or electrodeposited samples is probably due to the faster effective quenching from the vapour and the retention of the metastable phase over a wider composition range.

The ratios of the diameters, S_n/S_1, of the diffraction maxima, table 1, are, however, in close agreement with the predictions of a DRPHS model, and are very close to measurements of other single phase amorphous transition metal–metalloid glasses [11]. Also, the haloes do not appreciably change diameter in this composition range, which is also a feature reproduced in the DRPHS model, and is observed with sputtered Fe–Si alloys [12]. The extracted coherent intensity ratios of the maxima, I_1/I_n, as shown in table 1 (reproducible to within 20%) are also comparable with other studies [8]. These qualitative correlations suggest then that the Co atoms are able to arrange themselves in the, presumably, lower energy configuration associated with a dense, random packed structure.

Electron diffraction from an alloy with $x \sim 0.68$ gave a pattern, figure 6(c), with less obvious splitting of the second halo and a hint at the formation of a second amorphous phase by the presence of a faint halo with an effective $d = 0.316$ nm, which is close to the Si d_{111}, and a second faint halo from a possible amorphous Co silicide with an effective d-spacing of 0.260 nm.

For compositions $x > 0.8$, figure 6(d), the diameters of the diffraction maxima are as for those of pure amorphous Si, but the relative intensities are modified slightly. The effective d-values approximate to the Si {111}, {220} and {311} interplanar spacings and are consistent with a change to a CRN phase. There is no indication of any further structural change at lower Co concentrations. It is concluded that Co atoms incorporate substitutionally into the CRN of Si without the diffracting tetrahedral structures suffering any obvious distortion. This is possible because Co and Si have similar hard sphere diameters. This effect occurs with Fe–Ge alloys [13] where up to 20 at.% Fe can be accommodated into the Ge coherent random network without phase segregation.

3.1.4. Transmission electron microscopy. Representative planar TEM images for samples are recorded overfocus at low magnification in figures 7(a), (b) and (c). Figure 7(d) is taken underfocus. At low Si concentrations, figure 7(a), the film is composed of crystalline

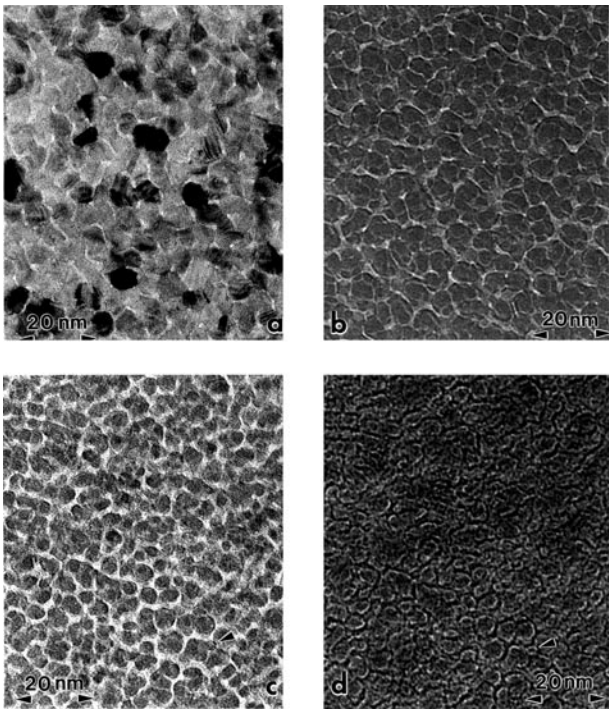

Figure 7. TEM micrographs for alloy films with (a) $x = 0.15$, (b) $x = 0.32$, (c) $x = 0.54$ and (d) as (c) but taken underfocus. The two single arrow heads in (c) and (d) mark the same feature.

grains with some evidence of lower density material at the grain boundaries. Adding Si decreases the number of strongly diffracting grains, and in figure 7(b) with $x \sim 0.32$ the uniform contrast in the grains suggests an amorphous structure, and the intergranular regions of uniform brighter contrast (and thus lower electron density) subsequently become far more obvious, e.g. figure 7(c). Both regions of the film are typical of an amorphous phase [14]. The Co-rich and darker patches or grains have diameters in the range 3 nm to 8 nm. The small changes in local atomic arrangements, indicated by the continuing presence of the shoulder on the second halo in the electron diffraction patterns for the composition range 30–60 at.% Si, appear to contradict the result that the film density/thickness changes substantially. This may be explained by the presence of compositional inhomogenities, specifically the formation of the low density channel structure clearly visible on a mesoscopic scale in these electron micrographs. This structure is expected to influence the properties of the films appreciably.

The morphology in figure 7(b) is common to many amorphous alloys and has been reported with sputtered Co–Si alloys containing relatively low levels of Si and grown on Si substrates [15], but with no explanation as to its origin. The brighter channels in figure 7 appear to increase in width as Si is added, but they never exceed about 2 nm in width and form a partial network that becomes connected as further Si is added. Clearly, the channel regions are of a lower electron density compared with granules. This may be due to several reasons. The first is the presence of mass fluctuations which can result from either void formation encouraged by a progressively reduced adatom mobility, or a strong surface roughness allowing a 'hill and valley' type surface. With this kind of morphology a contrast reversal is expected when

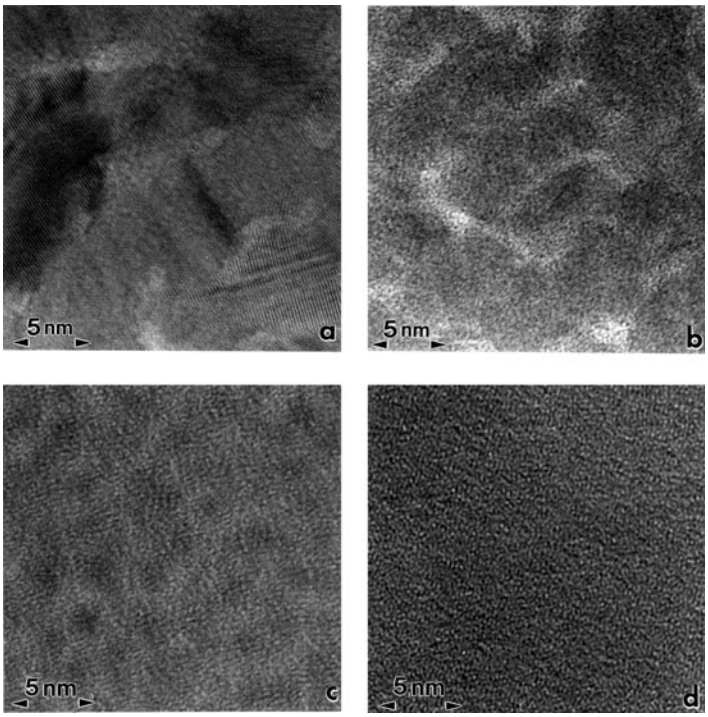

Figure 8. High resolution TEM micrographs (lattice imaging) of alloy films with (a) $x = 0.15$, (b) $x = 0.54$, (c) $x = 0.9$ and (d) $x = 1.0$.

images are taken under- and overfocus, as is observed in figure 7(c) and (d) though some segments of the channel remain unaffected (the small arrows mark the same part of the film). The second possibility is the presence of compositional fluctuations in which the boundary regions are richer in Si. It is possible that after some effective solubility limit in the grains segregation occurs which further establishes the network of channels. The third reason may be the establishment of a form of film growth in which columnar microstructural units are separated by less dense inter-columnar regions.

The fact the films are continuous and can be removed whole from the substrate would suggest that any possible void formation does not extend completely through the film, and surface roughness, usually occurring over smaller length scales, can also be rejected. This argument for a continuous, segregated microstructure is strengthened by what appear to be two intertwining channels of different brightness, best seen in the image of $Co_{0.68}Si_{0.32}$, figure 7(b), one scattering more strongly than its partner. The image is a summation of microstructures within the volume of the film, so what appear to be two independent networks is the same network but occurring at different depths within the film.

High resolution TEM images give clearer detail of the local microstructure. For compositions with $x < 0.20$, figure 8(a), large irregular Co alloy grains, identified by the lattice fringe spacing, are evident. The interfaces between the grains are indistinct and resemble the boundaries of nanocrystals, i.e. a gaslike structure with almost random interatomic distances [16]. In higher Si concentrations above the percolation limit ($x \sim 0.5$), well separated and darker amorphous (absence of lattice fringes) granular features form, figure 8(b). Although the thickness is increasing for these samples, the features do not appear to change size in

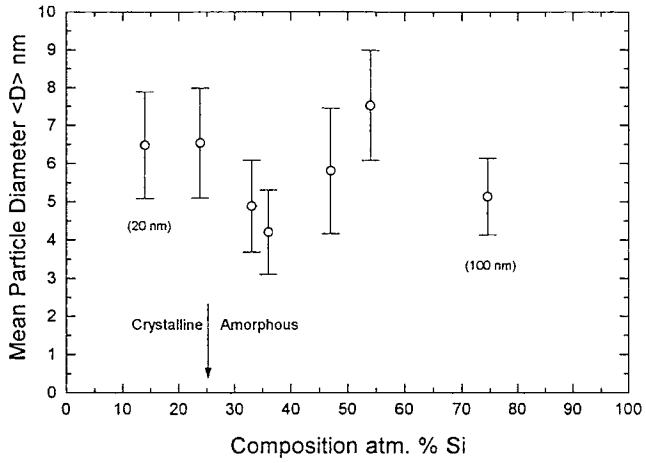

Figure 9. The change in the mean grain size with alloy composition. The numbers in the brackets and the error bars show the total film thickness and the FWHM of the grain size distribution. The results are taken from measurements of 300 grains in each micrograph.

any obvious manner with Si concentration. The form and contrast of the channels between the grains changes with increasing Si, from a distinct, although amorphous, form to, in figure 8(c), an indistinct second phase with a contrast similar to that for amorphous Si, figure 8(d). The dark patches in figure 8(c) suggest very small isolated clusters about 3 nm in size that would result from local concentrations of the heavier Co atoms incorporated in the Si CRN network. In general, measurements of grain or particle sizes in the TEM micrographs, figure 9, give fairly broad distributions with a trend to smaller average sizes at large values of x.

3.2. Chemical information

Observation of the ionization behaviour of the 3d transition metals by, e.g. ejection of the 2p electrons within the L shell, gives a method of sensing the occupancy of the conduction band. Such information is retrievable from PEELS spectra. Such spectra for Co–Si alloy films, convoluted and offset for comparison, are shown in figure 10. It can be seen that on alloying Co with Si, the Co L_2 and L_3 edges, corresponding to the displacement of $2p_{1/2}$ and $2p_{3/2}$ electrons into $3d_{5/2}$ and $3d_{3/2}$ states respectively, do not shift in energy but change in relative intensity, a result also found previously [17]. The degeneracy rule of the initial core electron state is given by $2J+1$. This predicts an electron transition probability ratio and edge intensity ratio of $L_3/L_2 = 2{:}1$, as observed in this work for pure cobalt.

Spectra are taken from a fairly large area of the film containing many grains and they will contain an average over the included grains and the channels between the grains. Although the channels may have a different composition to the grains they will contain far less cobalt, and a spectrum will, in the main, reflect the changes in condition of the cobalt content of the grains. Indeed, PEELS mapping of the 779 eV edge in the FEGTEM showed that the Co-rich films were characterized by a microstructure of Co-rich regions surrounded by regions depleted in Co. However, any contrasting distribution of Si was difficult to follow. EDX analysis also identified compositional inhomogeneities, with grains of approximately the expected composition surrounded by channels with a greater concentration of Si.

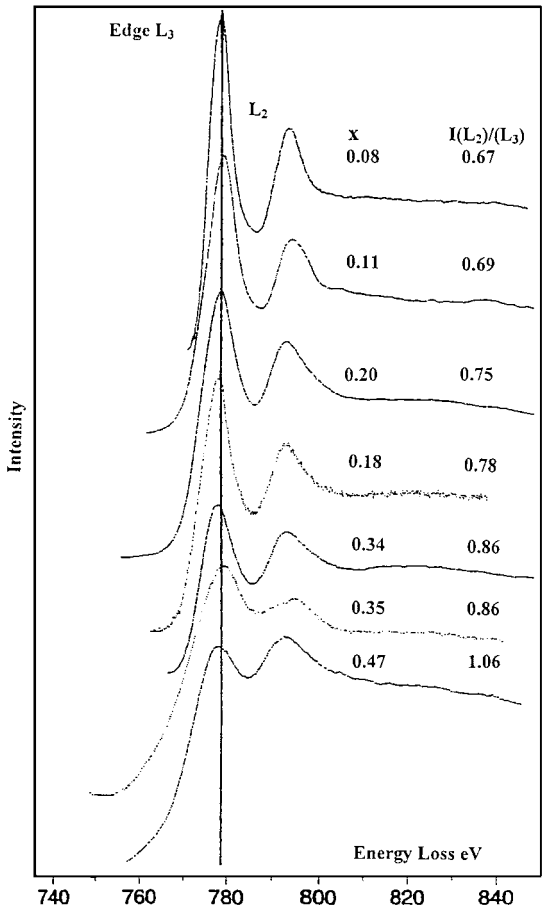

Figure 10. Transmission PEELS spectra at the $L_{2,3}$ edges of films with $0.08 < x < 0.47$. The offset curves are marked with the value of x and the ratio of the L_2 and L_3 edge intensities.

The edge intensity gives information on the valence occupation of the d-band. The intensities change across the transition metals, and copper, with its full d-band, has very weak edges. The apparent drop in both the L-edge intensities in figure 10 as Si is added indicates that the probability of electron transitions into the Co d-band reduces, suggesting that its occupancy is altering. Si is assumed to be divalent and to be able to donate electrons into the Co d-band. As with other magnetic transition metal–metalloid alloys (e.g. Ni–P), electron transfer to the magnetic atom can influence the average magnetic moment per metal atom and can also explain electrical resistivity behaviour.

The near-edge loss intensity of the spectra between ∼760 and 780 eV is also sensitive to excitations in to the conduction band states. These changes cause the peaks to broaden as Si is added. The edge spectra are averages for the environments of a large number of Co atoms, and the broadening could result from the fact that more Co atoms have a wider range of environments in alloys with greater Si concentrations. The indication of compositional inhomogeneities in the channel structure that appeared to increase as Si is added could be one source of this edge broadening.

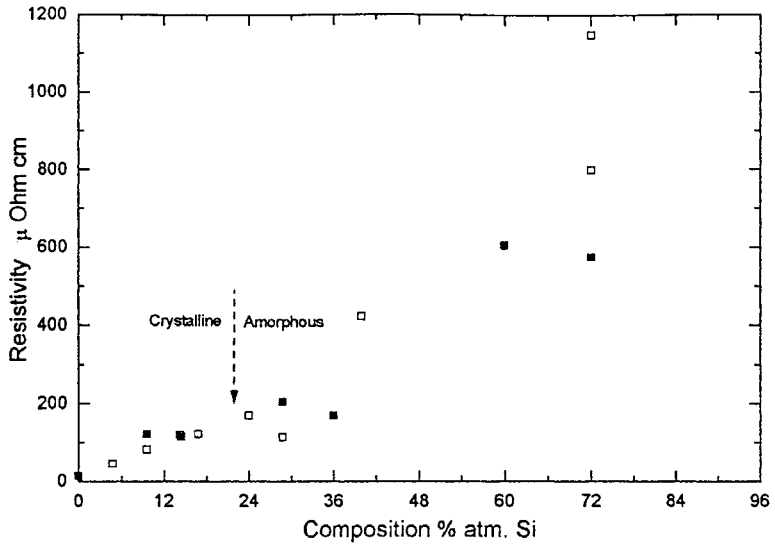

Figure 11. Showing the electrical resistivity of two series of alloys with $0 < x < 0.72$. The crystalline–amorphous division is marked in terms of the atomic percentage of Si.

4. Electrical resistivity and magnetic measurements

The room temperature electrical resistivity values, figure 11, are compatible with the structural changes suggested by the TEM study. The electrical resistivity of thin films above the dimensions of the mean free path increases with thickness to the bulk value. However, for sufficiently resistive thin films, where the mean free path is small and thicknesses change in the range 20 to 100 nm, that effect is negligible compared to those linked with compositional changes.

The resistivity of pure, bulk Co is $\sim$8 $\mu\Omega$ cm. For low Si concentrations of less than 10 at.%, relatively low values of resistivity of 10–50 $\mu\Omega$ cm are found, suggesting a metallic continuum and resistivities typical of metals doped with impurities. This rise in resistivity apparently reflects increased scattering from defects such as the incorporated atoms and the grain boundary area; the beginnings of the meandering channel structure observed at these compositions do not appear to be effective in significantly increasing resistivity. Around $x \sim 0.2$, when amorphization is first observed, the films have a resistivity of around 150 $\mu\Omega$ cm, which is a typical value for other amorphous metals or alloys [18]. Between 30 and 60 at.% of Si and in the DRPHS, resistivity increases appreciably, most likely as a result of the following structural changes. Co-rich regions become effectively isolated from each other by the channel structures as the percolation limit is approached. At the same time the average local environment of the Co atoms changes with composition, as evidenced by the PEELS results, and this affects the occupancy of the d-band. This is possible, even in the DRPHS arrangement which can also contain free atomic sites [11] allowing local changes in environment. Above $x \sim 0.7$ ohmic character is lost and above $x \sim 0.8$ towards pure silicon the electrical resistivity increases rapidly to more than 16 000 $\mu\Omega$ cm as the CRN is established.

Examples of ambient temperature ($\sim$300 K) magnetic hysteresis loops of a series of alloys are given in figure 12. Ferromagnetism, hysteresis and a finite coercivity are maintained up to about $x \sim 0.5$–0.6. Coercivity reaches a maximum of about 100 Oe at $x \sim 0.20$ when the

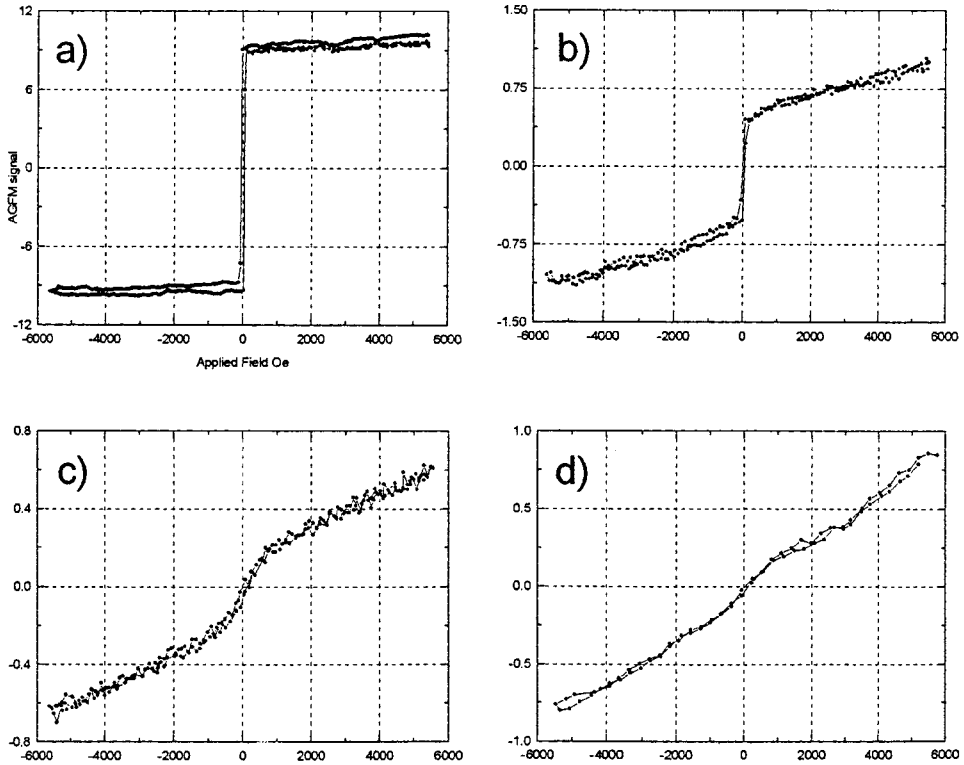

Figure 12. In-plane magnetic hysteresis loops taken at room temperature for (a) $x = 0.06$, (b) $x = 0.47$, (c) $x = 0.54$ and (d) $x = 0.70$. The AGFM signal is arbitrary.

sample is still crystalline, then falls rapidly with increasing Si concentration as the amorphous phase is established. Previous work [15] reports a maximum coercivity of ∼500 Oe in sputtered alloys with $x \sim 0.1$ attributed to a preferred c-axis orientation out of the plane of the film. This is compatible with the observations reported here, although the maximum in coercivity and the maximum in the 002 reflection occur at a higher Si concentration of ∼0.22. The films become difficult to magnetize to saturation beyond 40 at.% Si and yet the loops have a very low switching field, figure 12(b).

True superparamagnetism does not produce a narrow switching field distribution or an identifiable coercivity. The loop in figure 12(b) may be due to the coexistence of ferromagnetic and superparamagnetic phases that might originate in a large distribution of particle sizes or compositional inhomogeneities, e.g. possibly related to the granular and channel structures observed in the films. Similar effects have been reported previously [19]. For $x > 0.6$, a composition from which the electrical resistivity increases rapidly, figure 12, superparamagnetism is clear. Much lower initial susceptibilities characteristic of paramagnetism are observed for CRN structured samples with $x > 0.7$.

As shown in figure 13, increasing the metalloid concentration decreases the effective Co moment (pure Co is 1.8 μ_B) and also increases the L_2/L_3 PEELS edge intensity ratio in a fairly linear manner. Again, this correlation implies that electron transfer into the Co d band is responsible for the reduction in the Co moment. Measurements [20] on Ta additions to CoCrPt show the opposite behaviour, in that the Co L_2/L_3 edge ratio decreases linearly as the alloy is diluted with more Ta and the number of 3d Co electrons decreases from 8.1 to 7.9. An increase

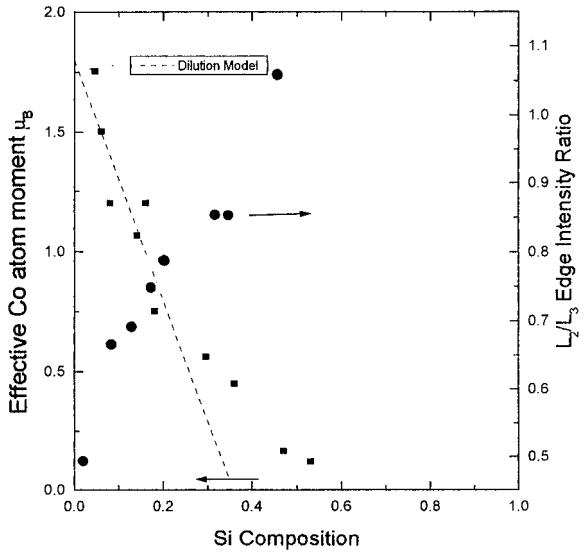

Figure 13. The Co magnetic moment (square symbols) and L_2/L_3 PEELS edge ratios (round symbols) as a function of $0 < x < 0.47$.

in Co moment is inferred and an experimentally determined reducing Curie temperature is related to a decreasing in the Co ferromagnetic exchange between adjacent Co atoms.

Several models have been proposed to describe the magnetism in metal–metalloid alloys, as reviewed in [21]. A covalent sp–d bond is assumed to from in a chemical dilution model [22] in which the concentration dependence of the moment is given by:

$$\mu = \mu_{Co}(1 - X(1 + 0.2Z_{B,A}))$$

where $Z_{B,A}$ is the maximum possible number of metal A neighbours about a metalloid B, X is the metalloid concentration and the bulk Co moment $\mu_{Co} = 1.8\ \mu_B$. With $Z_{Si,Co} = 9$, and assuming all Si valence electrons are transferred into the Co d band, this equation allows a qualitative comparison of predictions of the rigid band model with the measurements. This is shown in figure 13 by the dashed line. For other Co–metalloid combinations, i.e. there are no other reports for Co–Si alloys, the average Co moment is about $1\ \mu_B$ at a metalloid concentration of $x = 0.2$ [5, 23] in agreement with our findings here. This simple charge transfer model does not completely explain the compositional dependence of magnetic moment and it is clear that the details of the long range atomic arrangement in these systems should be introduced.

5. Conclusions

Sputter-deposited $Co_{1-x}Si_x$ alloy thin films have been investigated as part of a more detailed study of interface effects in Co/Si multilayers. Semi-quantitative analysis of diffraction information has allowed us to infer that the alloys change from an hcp crystalline structure through a non-crystalline DRPHS structure characteristic of metallic amorphous systems to a CRN structure typical of non-crystalline covalent metalloids across the composition range of $0 < x < 1$. Electrical resistivity measurements are compatible with the structural changes observed by electron microscopy, and show a change of values from those typical of crystalline and amorphous metallic thin film alloys to very large values in the amorphous CRN Si-rich phase. The room temperature variation of magnetic moment in the ferromagnetic phase for

$x < 0.4$ or 0.45 follows a simple dilution law and correlates with the details of electron transfer to the Co d band suggested by PEELS measurements. Between about $x = 0.45$ and 0.7 our investigations indicate the existence of more than one amorphous phase, with magnetic properties that suggest a co-existence of ferromagnetism and superparamagnetism originating in a wide distribution of particle sizes or compositional inhomogeneities possibly related to the granular and channel structures observed in the films. For $x > 0.7$ the room temperature measurements show that the alloys have a much reduced initial susceptibility and are apparently paramagnetic.

Acknowledgment

The authors thank Dr A Petford-Long of the Department of Materials, University of Oxford for confirmation of the local compositional inhomogeneities in these films.

References

[1] Grundy P J 1980 *J. Magn. Magn. Mater.* **21** 1
[2] Hansen P 1991 *Handbook of Magnetic Materials* vol 6, ed K H J Buschow (Amsterdam: North-Holland)
[3] Herzer G 1997 *Magnetic Hysteresis in Novel Magnetic Materials (NATO ASI Series 338)* ed G Hadjipanayis (Dordrecht: Kluwer)
[4] Fallon J M, Faunce C A and Grundy P J *J. Appl. Phys.* at press
[5] Cargill G S III and Cochrane R W 1973 *Amorphous Magnetism* ed H O Hooper and A M de Graff (New York: Plenum)
[6] Fullerton E E, Schuller I K, Vanderstraeten H and Bruynseraede Y 1992 *Phys. Rev.* B **45** 9292
[7] Yavari R, Nishitani S, Desre P and Chieux P 1988 *Z. Phys. Chem.* **157** 103
[8] Bagley B G and Turnbull D 1968 *J. Appl. Phys.* **39** 5681
[9] Bucher B Y 1972 *J. Non-Cryst. Solids* **7** 288
[10] Cargill G C III and Cochrane R W 1974 *J. Physique Coll.* **35** C4 269
[11] Elliott R J (ed) 1983 *Physics of Amorphous Materials* (New York: Longman)
[12] Mangin Ph and Marchal G 1978 *J. Appl. Phys.* **49** 1709
[13] Mangin Ph, Marchal G, Rodmacq B and Janot C 1977 *Phil. Mag.* **36** 643
[14] Hong Q Z, Barmak K and Clenenger L A 1992 *J. Appl. Phys.* **72** 3423
[15] Ishiguro T, Fujii H, Ichinese Y, Endo J and Harade H 1987 *J. Appl. Phys.* **61** 4284
[16] Birringer R 1989 *Mater. Sci. Eng.* A **117** 33
[17] Leapman R D, Grunes L A and Fejes P L 1982 *Phys. Rev.* B **26** 614
[18] James S 1976 *Appl. Phys. Lett.* **29** 330
[19] Dietz G and Schneider H D 1990 *J. Phys.: Condens. Matter* **2** 2169
[20] Sin K 1996 *J. Magn. Magn. Mater.* **155** 209
[21] Stein F and Dietz G 1989 *J. Magn. Magn. Mater.* **81** 294
[22] Pan D and Turnbull D 1974 *J. Appl. Phys.* **45** 1406
[23] Jaccarino V and Walker L R 1965 *Phys. Rev. Lett.* **15** 258